POLITECNICO DI TORINO
Repository ISTITUZIONALE

Bridging scales in multiphysics VCSEL modeling

(Article begins on next page)

23 April 2024

Bridging Scales in Multiphysics VCSEL Modeling

**Alberto Tibaldi, Jésus Alberto González Montoya,
Francesco Bertazzi, Michele Goano, Markus
Daubenschüz, Rainer Michalzik, Pierluigi Debernardi**

Abstract On our way to develop a comprehensive simulator of vertical-cavity surface-emitting lasers including carrier transport, optical modes, light-matter interaction and heat conduction, we address some critical multiscale aspects of the adopted coupling strategy. The quantum corrections to the semiclassical carrier transport framework are the bridge from nanometer to micrometer scales. In this paper, such corrections are shown to be fundamental in view of predicting the mode competition ruling VCSEL operation. Nevertheless, they can generate unforeseen features such as swirling electron flows in the active region, which are discussed here in detail. The simulation approach has been finally tested through a successful comparison with a large set of experimental results.

Keywords VCSELs · multiphysical simulation · optoelectronic device simulation · drift-diffusion

1 Introduction

More than 40 years after their conception, vertical-cavity surface-emitting lasers (VCSELs) are the standard semiconductor light sources in several applications such as short-range data

A. Tibaldi · F. Bertazzi · M. Goano · P. Debernardi
Istituto di Elettronica e di Ingegneria dell'Informazione e delle Telecomunicazioni, Consiglio Nazionale delle Ricerche, c/o Politecnico di Torino, Corso Duca degli Abruzzi 24, 10129 Torino, Italy

J. A. González Montoya · F. Bertazzi · M. Goano
Dipartimento di Elettronica e Telecomunicazioni, Politecnico di Torino, Corso Duca degli Abruzzi 24, 10129 Torino, Italy

M. Daubenschüz
Philips Photonics GmbH, Lise-Meitner-Straße 13, 89081 Ulm, Germany

R. Michalzik
Institute of Functional Nanosystems, Ulm University, Albert-Einstein-Allee 45, 89081 Ulm, Germany

E-mail: alberto.tibaldi@polito.it

communication systems, optical mice, printers or sensors [1]. The industry fascination of VCSELs is far from being exhausted, since they are conquering the automotive and smartphone markets as core elements for LiDARs or 3D cameras [2,3]. The VCSELs' success is to be ascribed to several key factors: on-wafer lasing and testing, low power consumption, high reliability and lifetime, and the natural possibility of array configurations. Nevertheless, aiming to expand the VCSEL horizon to the widest possible application range, their R&D is still among the liveliest branches of optoelectronics.

A major leap in this context would be producing VCSELs in the blue/green [4] as well as in the mid-infrareds [5–7], shifting the emission wavelengths from the well-established 850 nm window. However, re-investing for each material system the tremendous amount of time and resources that was necessary to commercialize AlGaAs devices is incompatible with today's design-to-market industrial policies. In this view, computer-aided design (CAD) could be strategic, allowing to avoid extensive prototype manufacturing campaigns.

Reproducing *LIV* curves requires to address the entangled interplay of electron transport, optical transitions, electromagnetic propagation and heat conduction by means of a multiphysics framework. While the thermal problem is quite standard and some solutions have been proposed for the determination of the VCSEL optical modes, the quest for the definitive carrier injection/optical generation description is still open. In fact, even if VCSELs are admittedly highly nanostructured, they really are three-dimensional macroscopic devices. While the solution of Maxwell's equations for the optical problem proved to be possible [8], simulating the entire structure by a fully quantum kinetic model at present is unfeasible from the computational point of view. A reasonable trade-off between accuracy and computational requirements is given by a drift-diffusion approach, complemented with photon rate equations.

The paper is organized as follows. Section 2 briefly describes the constitutive blocks of our in-house comprehensive VCSEL electro-opto-thermal numerical simulator VENUS. In particular, Section 2.2 focuses the discussion on the adequacy of the DD transport model to describe VCSEL operation, proposing different approaches for bridging from the micro- to the nanoscales. Finally, in Section 3 their impact in the attempt of reproducing experimental results is discussed in detail by showing the consequences of the quantum corrections.

2 Description of the electro-opto-thermal simulator

2.1 General overview

Our in-house comprehensive code VENUS features an optical mode solver, a description of the optical processes in the quantum well active region, a thermal simulator, and a carrier transport model.

To compute VCSEL modes might be very demanding. In fact, VCSELs feature hundreds of layers and in several applications their vectorial (polarization) characteristics are crucial. Therefore, completely-numerical approaches are to be discarded, also because the optical modes depend on the operation point, so that the optical solver has to be launched at least at every bias step. In this work, we apply our in-house 3D vectorial Vcsel ELectroMagnetic (VELM) code[8,9]. Exploiting the stacked structure of a VCSEL, VELM solves the longitudinal problem by means of a generalized transfer matrix method, where the 3D transverse geometrical features such as the oxide aperture or the device passivation are accounted for by coupled-mode theory. Similarly, all the other index variations are included by computing the corresponding coupling matrices. In fact, operation under strong pumping regime

requires to exploit "hot-VELM features" [10], which account in the whole VCSEL volume for the modified refractive index through the temperature profile. However, temperature has many additional effects, since it strongly influences the modal guiding and therefore rules also the transverse mode competition. The other important input from the drift-diffusion solver to VELM is the carrier profile, both 2D and 3D. In fact, 2D carriers influence the complex index profile (both real part, *i.e.* antiguiding, and imaginary part, *i.e.* gain). This is also the case for 3D carriers, which, in addition, rule free-carrier absorption effects.

The optical field is expanded in the cylindrical vectorial modes of a reference medium, exploiting the VCSEL axial symmetry. Beyond the two radiating sections, the device can be considered homogeneous, which leads to boundary conditions relating backward to forward waves. By enforcing the mode self-consistency condition of the field after a full-cavity round-trip an eigenvalue problem is obtained, whose complex eigenvalues represent the modal wavelengths and the corresponding threshold gains (real and imaginary parts, respectively). The corresponding eigenvectors are the expansion coefficients of the electromagnetic field in the cylindrical wave basis and allow to compute the optical modes everywhere. VELM proved its reliability as an optical CAD tool by assisting the analysis and design of several VCSELs, such as: standard [11], non-circular/anisotropic [12], phase-coupled array [13], polarization-stable [14], high-contrast grating [6, 15–17] and spiral phase plate [18] devices.

The first step to describe the conversion of the carriers into coherent and incoherent photons in the VCSEL active region is the evaluation of the quantum well subbands. A fair compromise between accuracy and computational cost is given by multiband $\mathbf{k} \cdot \mathbf{p}$ envelope-function models. More specifically, the nanostructure is described by a finite element method (FEM). The unphysical spurious subbands have been eliminated by the approach proposed in [19], based on representing correctly the projections of the differentiation operators [20]. Under the assumption of axial invariance, the Hamiltonian is block-diagonalized, leading to a 4-band formulation (heavy holes, light holes, split-off and electrons). The spin degeneracy is accounted for in the evaluation of the stimulated and spontaneous emission processes, which is performed by Fermi's golden rule. The scattering relaxation is phenomenologically introduced in terms of a lineshape broadening, including non-Markovian features [21]. Finally, this approach is refined with a many-body description of the carrier-induced band-gap renormalization.

Simulating heating phenomena in VCSELs is a delicate task, due to the entangled temperature dependence of several model parameters. For example, reproducing the thermal roll-over is difficult, since it requires the correct description of the thermally-dependent non-radiative recombinations, transverse mode interactions and optical absorption processes. In this work the temperature profile is obtained by solving the heat equation by means of a spectral element method (SEM) [22, 23]. The domain of the heat equation is separated into few sub-domains, where the thermal conductivity is assumed constant. In particular, in the substrate, thermal sources are nearly z-independent, leading to almost-linear temperature variations, while in the active part strong temperature gradients are observed. SEM permits to define a set of local basis functions in every subdomain, each with different numerical resolution. This allows to describe with the optimal basis each part of the VCSEL, leading to a very fast and accurate temperature profile evaluation.

A reasonable physics-oriented approach overcoming the limits of phenomenological carrier rate equations but more computationally-affordable than high-order semiclassical techniques [24–26] or genuine quantum approaches [27, 28] is the drift-diffusion model [28, 29], which consists of the quasistatic Poisson's equation coupled selfconsistently to the carrier continuity equations:
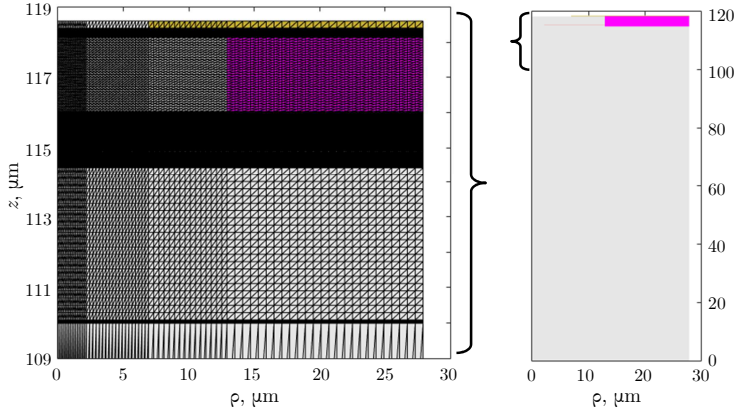
Fig. 1 Device cross-section, limited to the drift-diffusion computational window, illustrating the main transverse features of the device under analysis. Left: longitudinal zoom of the VCSEL active region. Right: entire simulated device, including the $110\,\mu$m thick substrate.

$$\begin{cases} -\nabla^2\phi = \dfrac{q}{\varepsilon}\left(p - n + N_{\mathrm{D}}^+ - N_{\mathrm{A}}^-\right) \\[2mm] \dfrac{\partial n}{\partial t} = \dfrac{1}{q}\nabla\cdot\mathbf{J}_n - U_n \\[2mm] \dfrac{\partial p}{\partial t} = -\dfrac{1}{q}\nabla\cdot\mathbf{J}_p - U_p. \end{cases} \tag{1}$$

The model unknowns ϕ, n and p are the potential and the electron and hole densities. The quantities N_{D}^+ and N_{A}^- are the ionized donor and acceptor doping concentrations, while $\mathbf{J}_n$ ($\mathbf{J}_p$) and U_n (U_p) indicate the electron (hole) current density and net electron (hole) recombination terms. The elementary charge and the static dielectric constants are indicated with q and ε. In this work, the static nonlinear drift-diffusion system is solved by a generalized Newton method, where the numerical instabilities caused by the advective nature of the current constitutive relations [30] are addressed by applying the Scharfetter-Gummel approach [31]. To predict lasing operation, this *basic* model must be augmented with rate equations relating the gain G_q, the losses L_q, the spontaneous emission S_q and the stimulated emission power $P_{\mathrm{st},q}$ for each q-th VCSEL mode:

$$\frac{\partial P_{\mathrm{st},q}}{\partial t} = \Gamma_z\left(G_q - L_q\right)P_{\mathrm{st},q} + \Gamma_z S_q, \quad q = 1,\ldots,N_{\mathrm{modes}}, \tag{2}$$

where Γ_z indicates the longitudinal confinement factor [32]. The inherent instability of the photon rate equation arising at the transition to lasing operation has been tackled by requiring, as an additional constraint, $P_{\mathrm{st},q} > 0$. This strategy drives the Newton loop far from the *wrong* solution, and it could be required every time a VCSEL mode starts lasing.

Among the VENUS constituents, only the electrical solver is based on an extensive spatial discretization, whereas both thermal and optical solvers are based on modal expansions. For this reason no grid adaptation is required at all, reducing the multiphysics couplings to the simple evaluation of the optical and thermal quantities on the drift-diffusion mesh points. The coupling between electrical and optical/thermal simulators is included at the end of each voltage step, so the electric, optical, and thermal simulations are not solved in

a strictly self-consistent fashion. However, this approach is nearly exact when the voltage increment is sufficiently small. While before appreciable current flows, a 200 mV step is appropriate, describing lasing operation and the consequent self-heating accurately requires steps not exceeding 20 mV. Figure 1 shows a typical VCSEL discretization. The gold and purple regions indicate the p-contact and the passivation, respectively. A region with a very dense mesh can be noticed, which corresponds to the active region and to the first DBR pairs close to it. It is known that, far from the active region, the DBR layers can be replaced with an effective average material [33]. Additional details about the VENUS workflow can be found in [34].

The primary limitation of this model is its semiclassical nature, so that it is not suitable for simulating nanostructures. For this reason, the following section will discuss a micro/nano-scale bridging strategy, emphasizing advantages and possible contraindications.

2.2 Bridging micro- to nano-scales by quantum-corrected transport models

From the charge carriers perspective, a VCSEL is a complex environment where the current-carrying extended states, after being transported through the DBR and substrate bulky regions, interact in the nanostructure with localized states, which are involved in the optical emission processes. Even if describing adequately such an entangled interaction would require quantum kinetic formalisms such as the non-equilibrium Green's function (NEGF), studying an entire micro-scale device with the present computational resources is unthinkable, leading to the trade-off described in the previous Section.

With the aim to bridge the micro- and nano-scales, several groups from the early '90s proposed semiclassical (and specifically drift-diffusion) approaches for semiconductor laser simulation, augmented with quantum corrections describing the bound-bulk carrier interactions. Among seminal works it is worth mentioning those by the Eisenstein [35], Baraff [36, 37], Alam [38, 39] and Hess [40] groups. The latter has been adopted in the multiphysics simulators developed by the Fichtner group [41, 42], and is still a topical subject [43–45].

Inspired by these works, the authors recently developed a quantum-corrected drift-diffusion (QCDD) code [28, 46, 34], where bulk carrier transport is described by standard continuity equations. Instead, bound carriers can move freely only in the lateral quantum well direction:

$$\begin{cases} \dfrac{\partial N^{2D}}{\partial t} = \dfrac{1}{q}\nabla_t \cdot \mathbf{J}_{N^{2D}} - U_{N^{2D}} \\ \dfrac{\partial P^{2D}}{\partial t} = -\dfrac{1}{q}\nabla_t \cdot \mathbf{J}_{P^{2D}} - U_{P^{2D}}, \end{cases} \tag{3}$$

where ∇_t denotes differentiation along the lateral QW direction, and N^{2D}, P^{2D} are the bound carrier densities. In Poisson's equation, these charges are distributed on the confined direction according to an envelope function obtained from the solution of Schrödinger's equation:

$$-\nabla^2\phi = \frac{q}{\varepsilon}\left(p - n + \sum_i P_i^{2D}\left|\Psi_i^p\right|^2 - \sum_j N_j^{2D}\left|\Psi_j^n\right|^2 + N_D^+ - N_A^-\right). \tag{4}$$

The envelope eigenfunctions are defined on the entire VCSEL domain, so that Poisson's equation takes into account also the eigenfunction tails into the barriers. The eigenfunctions are normalized according to

$$\int_{VCSEL}\left|\Psi_i^p(z)\right|^2 dz = \int_{VCSEL}\left|\Psi_j^n(z)\right|^2 dz = 1. \tag{5}$$

In the following we provide just a quick description of this model, focusing on how to bridge the bulk-bound carriers. Additional details can be found in [28,46].

The quantum capture/escape dynamics are described through a recombination rate similar to that of [36,37,40]:

$$
\begin{aligned}
C_n^{\text{cap}} &= \underbrace{\left[1 - \exp\frac{E_{\text{F},n}^{\text{2D}} - E_{\text{F},n}^{\text{3D}}}{k_\text{B}T}\right]}_{\text{capture/escape}} \underbrace{\left(1 - \frac{N^{\text{2D}}}{N_2}\right)}_{\text{2D states filling}} \underbrace{\frac{n}{\tau_{\text{scat},n}}}_{\text{capture}} \\
C_p^{\text{cap}} &= \left[1 - \exp\frac{E_{\text{F},p}^{\text{3D}} - E_{\text{F},p}^{\text{2D}}}{k_\text{B}T}\right] \left(1 - \frac{P^{\text{2D}}}{P_2}\right) \frac{p}{\tau_{\text{scat},p}}
\end{aligned}
\tag{6}
$$

These terms act as a coupling between the bulk and bound drift-diffusion equations, since they are added to U_n (U_p) and subtracted from $U_{N^{\text{2D}}}$ ($U_{P^{\text{2D}}}$). Focusing on electrons, $E_{\text{F},n}^{\text{3D}}$ and $E_{\text{F},n}^{\text{2D}}$ indicate the bulk and bound quasi-Fermi levels and N_2 is the maximum density that fits into the QW bound states [28,42,46]. At thermodynamic equilibrium, the 2D and 3D quasi-Fermi levels are equal, so that the net capture is zero (first parenthesis in (6)). Depending on the injection condition, (6) can describe either capture or escape of bound carriers, as a consequence of $E_{\text{F},n}^{\text{3D}}$ being below or above $E_{\text{F},n}^{\text{2D}}$. The second parenthesis (state filling) has the physical meaning that the QW can capture carriers until it is full; beyond that level, the carriers escape from it. The scattering time $\tau_{\text{scat},n}$ takes into account all the scattering processes in a phenomenological fashion, such as those generated by carrier-phonon and carrier-carrier interactions, impurities and surface roughness [40]. Therefore, this parameter governs the conversion rate of 3D↔2D carriers, and it is used in this work to fit and interpret the experimental results. In future works it might be extracted from NEGF simulations.

Figure 2 describes the role of C_n^{cap} for a one-dimensional mesh. The bound and bulk carriers are assumed to be separated in energy, which corresponds to identify as bound carriers those with energies lower than the barrier. This is enforced by evaluating the 3D carrier densities in the QWs by means of Fermi integrals starting from the energy corresponding to the barrier material, as shown in Fig. 2 for electrons. So, the carriers on the *green nodes* can be either scattered into the QW through the capture term or move by drift-diffusion, contributing to thermionic current [47].

3 Insights and outcomes of the quantum-corrected approach

This section describes the application of VENUS to the simulation of an oxide-confined Al-GaAs VCSEL designed and manufactured at Philips Photonics. The investigated device has the following characteristics: the 1λ-cavity is equipped with three 8 nm GaAs QWs, placed at the peak of the optical standing wave. The 30 nm oxide layer with $4\,\mu$m aperture diameter is placed in the first of the 21 pairs of the p-DBR outcoupling mirror. The bottom DBR includes 37 pairs. All the mirror pairs are subjected to composition and doping gradings to optimize the conduction features and, at the same time, to keep the free-carrier absorption losses at a minimum. The devices under investigation show a good circularity and low birefringence, so no particular feature shows up, such as those observed, *e.g.*, in [12]. Therefore VENUS, which treats the transport of axisymmetric structures, can be safely applied. The VCSEL ground contact is connected to a heat sink, whose temperature can be set to a certain value. This allowed to perform experimental characterizations emulating 20 °C, 50 °C, 80 °C and 110 °C ambient temperatures.
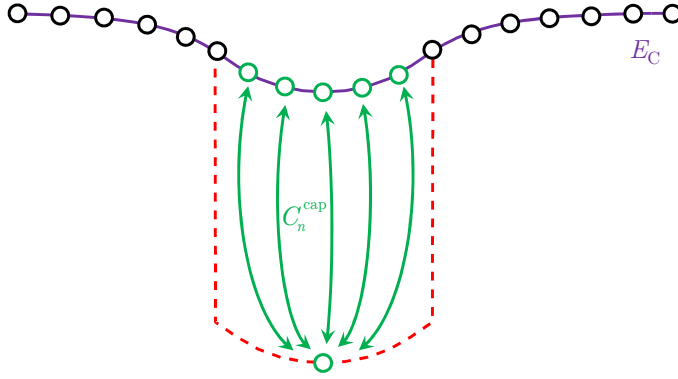
Fig. 2 Sketch of the adopted quantum correction for the conduction band. The green circles indicate the mesh points involved in the process. The solid purple and dashed red curves identify the band structures for bulk and bound carriers.

A large set of experimental results is available for each of these conditions: in addition to the *LIV* characteristics, this includes several optical spectra measured at different injection currents. Such data allows to keep track of the temperature increase by measuring the wavelength red-shift, and to evaluate the modal power information, disclosing which transverse mode is lasing and in which proportion to the other ones [48]. In this work we focus on $50\,^{\circ}$C heat sink temperature, which is an intermediate condition among those available from the experiments.

Due to the $4\,\mu$m diameter oxide aperture, the VCSEL under investigation supports mainly the fundamental (LP_{01}) and the first higher-order (LP_{11}) modes, while the second higher-order mode (LP_{02}) appears just before the VCSEL switch-off, so that one of the main modeling challenges is the correct prediction of the transverse mode competition. Mode competition is governed by spatial hole-burning, which distributes gain differently to the transverse modes at increasing optical power: the spatial hole is dug according to the modal field intensity profiles and re-filled by the motion of carriers. This is why QW carrier mobility is the most important model parameter ruling spatial hole-burning: if diffusion were infinite, no spatial hole could be observed while, with low mobility, mode competition would be exclusively ruled by the optical VCSEL features.

Spectral hole-burning effects are included in the simulation framework as well, in terms of a gain compression factor. Although this is known to impact on VCSEL dynamics, it does not affect significantly the *LIV* static characteristics [1]. Future works will deal with the impact of spectral hole-burning on the VCSEL dynamic/noise characteristics.

Besides providing a realistic longitudinal profile of the space charge (related to the carrier eigenfunctions of (4)), the quantum corrections described in Sect. 2.2 are an essential tool to enhance the description of carrier transport in the active region. To demonstrate this point, Fig. 3 reports a comparison of simulation results obtained with a simplified VENUS implementation where the QWs are treated as standard, *bulk* heterostructures [47] (a)–(c), and with quantum corrections (d)–(f). The experimental results are indicated with black dots in the *IV* and *LI* characteristics and as open bullets in the modal power contributions. In these simulations, the electron mobility in the VCSEL QWs is reduced parametrically by a factor of 20, 5 and 1 (nominal bulk value). Instead, the mobility of holes, already lower than that of electrons by a factor of 20, is kept at the nominal bulk value.
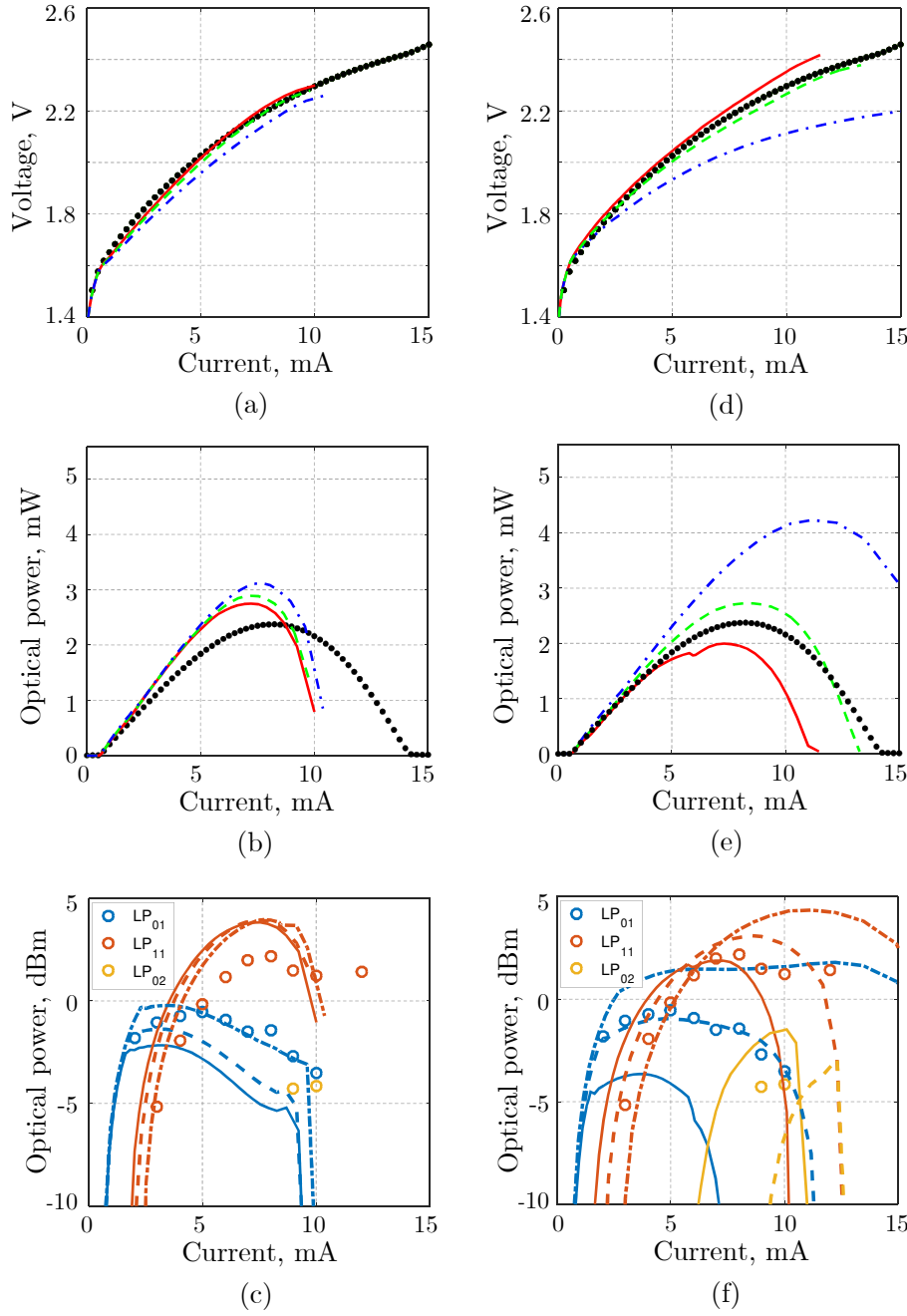
Fig. 3 Comparison of VENUS simulations with experimental results. Figures (a)–(c) and (d)–(f) are obtained with bulk and quantum-corrected simulations, respectively. The three simulations are obtained for different QW mobilities, which are multiplied by a factor 0.05 (dash-dotted curve), 0.2 (dashed curve), and 1 (solid curve). In the *IV* (a), (d), and *LI* (b), (e) characteristics, the different simulations have been also identified with different colors, to help comparison with the experiments (black dots). Subplots (c) and (f) focus on the competition between the LP_{01} (blue), LP_{11} (red) and LP_{02} (yellow) modes.

In the quantum-corrected simulations (d)–(f), the effect of a reduced mobility is very strong on both the electrical (*IV*) and optical (*LI*) features. In fact, at around 2.2 V, using the bulk mobility (blue curves) would imply doubling the current and a completely wrong *LI* curve, with a doubled optical power and a delayed roll-over. A strong impact can also be observed in the modally-resolved output powers (d): the overestimated bulk mobility prevents the spatial hole from being dug, so the fundamental mode (LP$_{01}$) is dominant over the whole operation range, the first-order mode (LP$_{11}$) experiences a delayed start, and the third mode (LP$_{02}$) never shows up. From these numerical experiments we can conclude that the mobility in the QWs must be around one fifth of that of the bulk.

On the contrary, the bulk simulations (a)–(c) are characterized by a strong insensitivity of the *LIV* characteristics on the QW mobility. More in detail, the bulk *IV* characteristics are not too different from the measured ones, even if they exhibit an angular point in correspondence of the optical threshold. Changing the mobility has no impact on the initial slope of the *LI* curves, which is quite close to that of the quantum-corrected simulation with bulk mobility. Moreover, this leads just to a 10% variation of the optical power compared to its maximum, with a marginal effect on the earlier and faster roll-over. This implies that, without quantum corrections, it is not possible to reproduce adequately the experimental results. The modally-resolved powers (f) confirm this trend, exhibiting a minor impact of the mobility change, giving no chance to the LP$_{02}$ mode to appear.

Carrier mobility has been deeply investigated for bulk GaAs [49] and proved to be a complex topic. In fact it depends, besides alloy composition, on doping concentration [50]. Heating plays a relevant role as well, since the internal temperature increase in these devices is of the order of 100 °C that, added to the heat sink temperature, can reach a total of about 200 °C. A large body of work has been devoted to the study of mobility in two-dimensional electron gases (2DEGs), with the aim of optimizing lateral transport in high electron mobility transistors (HEMTs). In this context, it is well known that surface roughness scattering from the well-barrier interfaces is an important mobility limiting scattering mechanism, strongly dependent on the QW width, barrier composition and growth condition. In fact, in narrow quantum wells, interface irregularities cause strong fluctuations in the confinement energies, which are known to drastically reduce the electron mobilities, as also observed from our simulations [51,52]. The main difference between the HEMT channel and the VCSEL active region is that in the QWs both electrons and holes are present. In this view, also Coulomb scattering contributes to the detriment of carrier mobility [53].

The fundamental role of quantum corrections might seem surprising, especially if we think that they are applied just to the three 8 nm QWs. However, since QWs are the strongest recombination centers of the device, it is reasonable that disabling the vertical transport channel across the nanostructure emphasizes the importance of motion along the only direction allowed, and in general affects the carrier dynamics. The phenomenological scattering times $\tau_{\mathrm{scat},n/p}$ in (6) allow to tune the effects of quantum corrections. This is demonstrated in Fig. 4, which reports the *LIV* characteristics simulated by varying parametrically the electron and holes scattering times. More in detail, Fig. 4(a) shows that fast capture dynamics, described with short scattering times, resembles the bulk scenario, as emphasized by the angular point in the *IV* characteristics at the optical threshold just like in Fig. 3(a). In this view, the quantum correction can be interpreted as some sort of additional *latency* introduced in the carrier dynamics and not applicable to the classical heterostructure treatment [47]. Too much latency inhibits the 3D–2D carrier exchanges, affecting both the electrical and the optical characteristics. The results of Fig. 4 suggest to use scattering times of the order of 10 ps at most, which are compatible with the results presented in the literature [40].
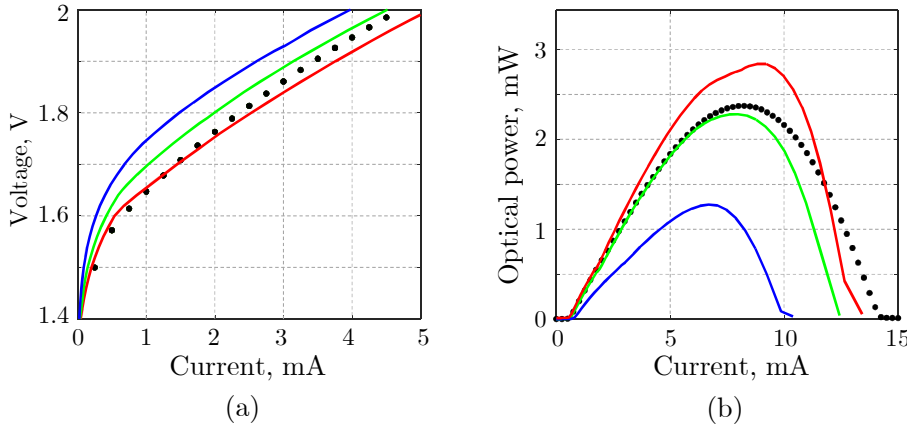
Fig. 4 Investigation of the effect of the electron capture time on the electrical (a) and optical (b) device performance. Red, green and blue curves refer to capture times of 1, 10 and 50 ps, respectively.

Since VENUS is an in-house software, it provides access to several intermediate quantities, such as those reported in Fig. 5, in the proximity of the active region. The (a)–(c) and (d)–(f) plots report bulk and quantum-corrected results, respectively. Focusing on the carrier density plots (a) and (d), one effect of the quantum corrections can be immediately noticed: the peaks, each one corresponding to a QW, are much smoother in the quantum-corrected than in the bulk simulations, since the former are distributed according to the envelope eigenfunctions, as shown in (4). Subfigures (b) and (e) report the electron (blue), hole (red) and total (green) currents. The green curves demonstrate that our approaches conserve the total current in any longitudinal section, as obviously dictated by the conservation law. Just like the carrier density plots, also these figures allow to identify the QWs as the regions where electron current is converted into hole current. Such phenomenon is related to the (mainly radiative) recombination phenomena occurring in the QWs, modeling the conversion of carriers into photons. The presence of minority currents at the sides of the cavity can be noticed, which indicate an incomplete conversion; this is commonly referred to as the leakage current. Finally, subfigures (c) and (f) report the electron (blue) and hole (red) current vector plots for the bulk and quantum-corrected simulations, respectively. These vector plots are strictly connected to (b) and (e), which are obtained by computing their flux integrals at each longitudinal section.

Figure 5(f) highlights a rather peculiar phenomenon. While the bulk current plot (c) shows the typical hole into electron current conversion, its quantum-corrected counterpart features an *electron vortex*: both hole and electron current densities point towards the active region, and the electron current exhibits a swirling motion supported by lateral transport in the QW. Being alerted about this unusual current flow, which seems to suggest the presence of unphysical generation terms in the proximity of the QW, a detailed investigation of the VCSEL recombination rates in the active region has been carried out. By this way it was possible to find that, in the lasing operation injection regime, the electron and hole recombination terms are locally different, dominated by the bulk-bound scattering terms (6). In the case of electrons these are negative, which corresponds to a net carrier escape and then to a generation term for bulk carriers. This is shown in Fig. 6(a), which reports the QW electron (blue) and hole (red) capture terms assuming nominal bulk electron mobility in the QW
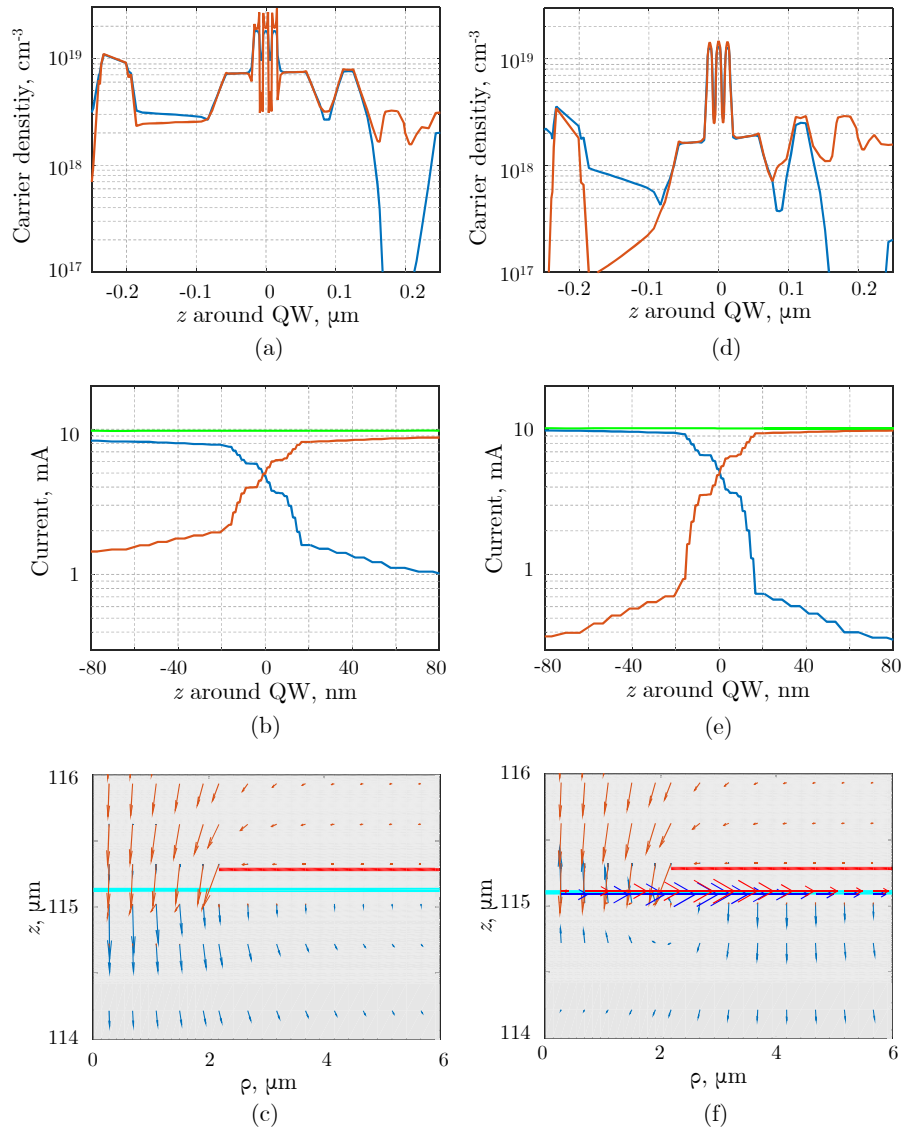
Fig. 5 Detailed results from the simulation of the reference VCSEL, without (a)–(c) and with (d)–(f) quantum corrections, at an injection of 10 mA. Subfigures (a) and (d) report the carrier densities on the device axis around the central QW (set as coordinate reference). Subfigures (b) and (e) show the flux integrals of the electron (blue) and hole (red) current densities for each longitudinal direction; the green line is their sum. The vector plots (c) and (f) show the electron (blue) and hole (red) current densities in the proximity of the active region.
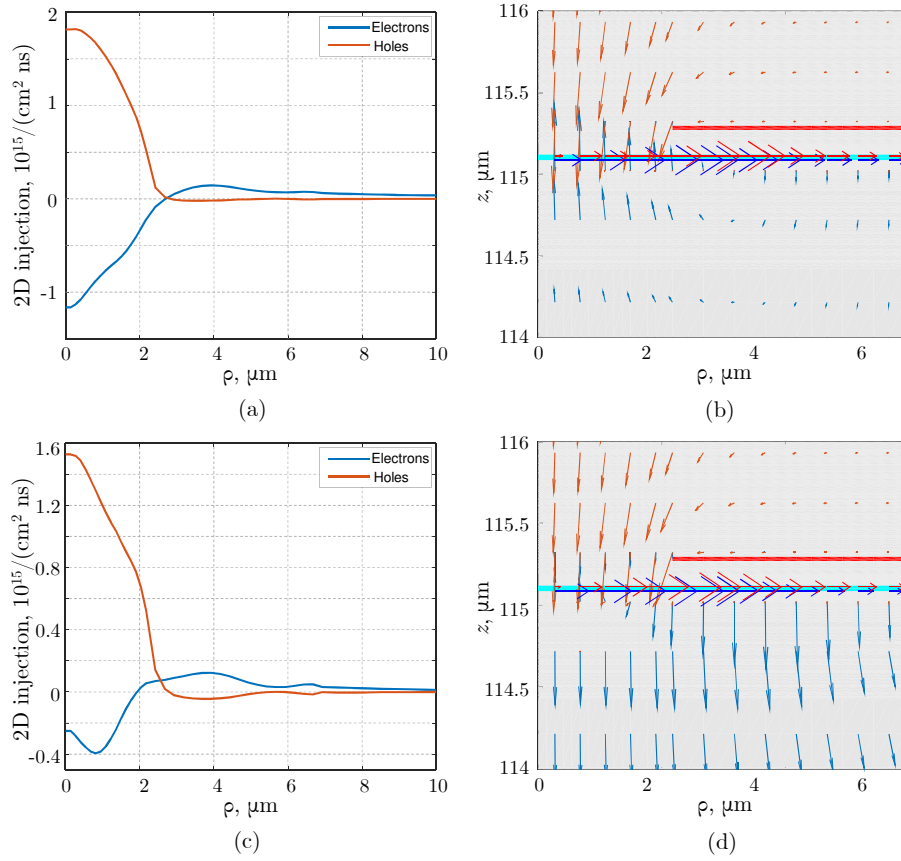
Fig. 6 Left: carrier capture radial profiles. Right: carrier density vector plots. Blue and red curves refer to electrons and holes, respectively. Subfigures (a) and (b) have been obtained assuming bulk mobility also in the quantum wells, whereas in (c) and (d) it has been multiplied by a factor 0.05.

(such as in the blue dashed-dotted curves in Fig. 3). Correspondingly, Fig. 6(b) clearly shows the electron vortex with the current density that flows towards the active region, moves laterally in the QW and escapes at higher distance from the VCSEL axis.

Even if this phenomenon could be at first regarded as unphysical, no inconsistency can be found in the model. First of all, VENUS does not rely on the $n = p$ approximation typical of rate equation solvers, because the electron and hole transport parameters (density of states and mobility) differ significantly: this justifies local differences between electron and hole densities. However, global neutrality is satisfied in VENUS. In fact, if the volume integrals of the generation/recombination terms were different, the current could not be conserved. As already shown in Fig. 3(b), current is conserved through the active region, which demonstrates that the integrals (in cylindrical coordinates!) of the electron and hole capture rates in Fig. 6(a) are equal. As it can be seen by integrating the continuity equations in (1), current conservation implies that the electron and hole recombination integrals are equal. Since Shockley-Read-Hall, radiative and Auger recombinations are locally equal for electrons and holes, the capture term integrals must be equal.

The role of lateral diffusion in this phenomenon is demonstrated by Fig. 6, which compares the simulation results for an electron QW mobility equal to the bulk value (Figs. 6(a,b)) and reduced to 5% of the bulk value (Figs. 6(c,d)). A lower QW mobility leads to a lower escape (see Fig. 6(c)) and, correspondingly, to a much mitigated electron vortex effect (just a few blue arrows can be noticed below the oxide aperture). In fact, lateral transport in the quantum well is influenced by the positive electrostatic field, peaking at the oxide aperture, which acts as a driving force for QW electrons, moving them towards the VCSEL axis. The generation of such QW excess electrons, which increase when higher electron mobilities are assumed, explains the negative capture rates. The impact of a negative capture on current density can be grasped easily if we consider the current continuity equation reduced to 1D:

$$\frac{1}{q}\frac{\partial J_n}{\partial z} = U_n.$$

(7)

It is clear that the current decreases in presence of negative net recombinations, which is the case of carrier escape on the VCSEL axis ($\rho = 0$) and is somehow similar to what happens in photodiodes under illumination. This effect does not influence only the active region since, in highly-pumped regimes corresponding to strong carrier escape, some space is required for current to recover its "usual" behavior.

An experimental observation of the electron vortex could be potentially obtained from an imaging of the spatially-resolved current densities inside the device. At present such measurements are performed on 2D materials such as graphene [54–56], but in the past they have been also applied to GaAs/AlGaAs heterostructures [57,58]. However, to the best of our knowledge, they have never been attempted on a complex device such as a VCSEL, where the active region is buried below several layers. An alternative validation could be based on more sophisticated simulation frameworks such as the non-equilibrium Green's function approach, even if at present it could be hardly applied to an entire VCSEL.

Having gained this experience on multiphysics modeling and after a thorough calibration procedure of the models presented in Appendix A, which led to the parameters reported in Table 1, it was possible to achieve a satisfactory agreement with the experimental results, reported in Fig. 7. The excellent comparison of the electrical properties, evident from Fig. 7(a), is strengthened by Fig. 7(d), which shows the differential resistance versus voltage. This is a much more sensitive quantity than the *IV* curve, due to its differential nature. Fig. 7(b) reports the QW carrier concentrations versus current. Even if this quantity cannot be related directly with experimental results, it provides a first indication of the causes of the VCSEL switch-off. It could be seen that, at the roll-over, 3D carriers (specifically electrons) start to grow quickly. This is a consequence of the drop of the stimulated emission, which corresponds to a rise of other recombination terms. This is especially true for Auger processes [34,59–62], which are identified as fundamental mechanisms limiting lasing operation. The wavelength red-shifts reported in Fig. 7(e) are the *thermometers* of the VCSEL, since they are directly related to the temperature increase in the device; in this view, this excellent comparison corroborates the correctness of the VENUS thermal modeling. Finally, understanding the role of the quantum corrections on the lateral transport was crucial in view of reproducing the optical VCSEL properties. This is certainly important for the total optical power, reported in Fig. 7(c), but also for individual modal contributions, as shown in Fig. 7(f), which demonstrates a very good prediction of the multimode competition occurring in the VCSEL.
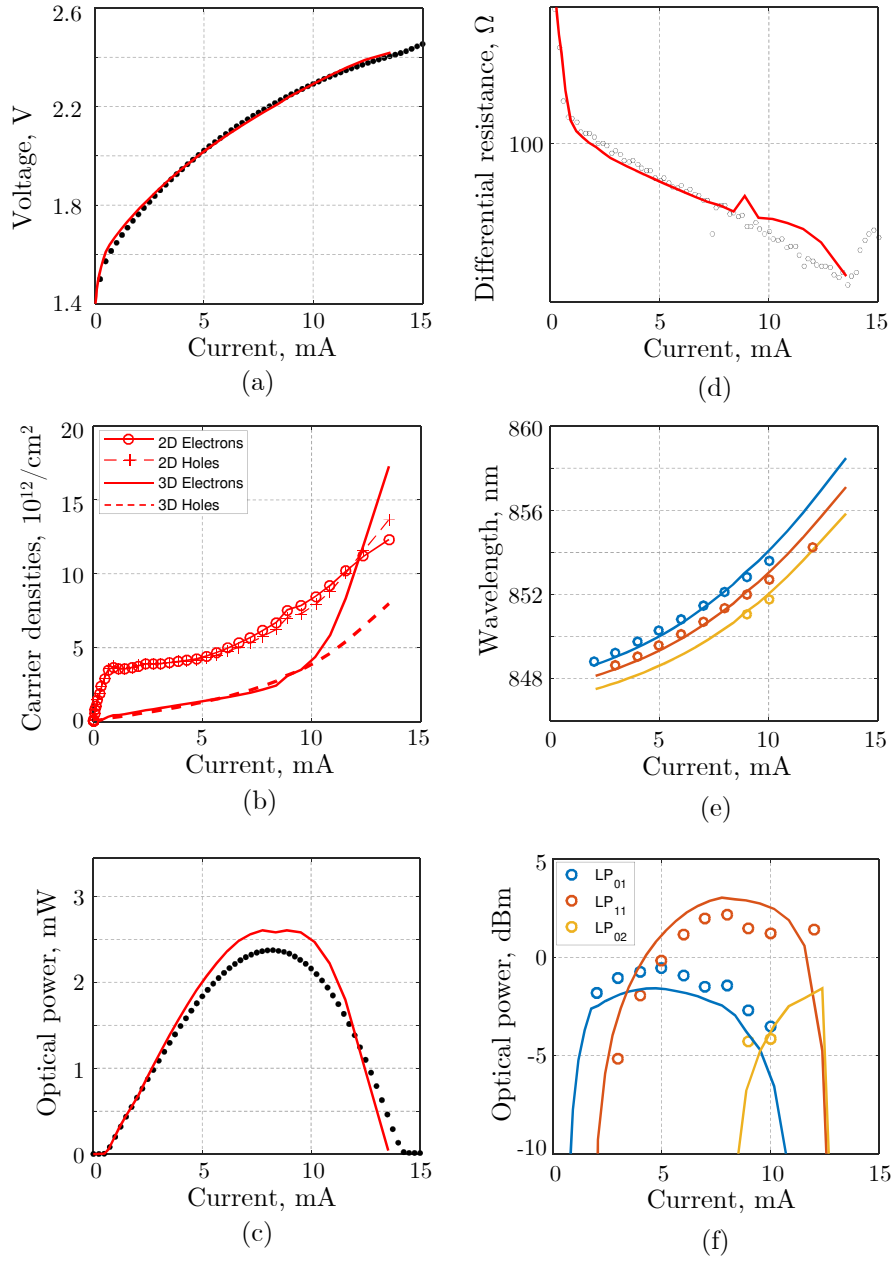
Fig. 7 VENUS output chart, reporting also the experimental results of the VCSEL under analysis ($4\,\mu$m oxide aperture at $50\,°$C). The chart features: *IV* characteristics, 3D and 2D carrier densities at the QW center (the only quantities not directly observable from experiments), *LI* characteristics, differential resistance, modal wavelengths and lasing powers. The experimental results are indicated by dots or open circles, VENUS outputs with continuous lines.

Table 1 Transport, thermal and optical parameters of $Al_xGa_{1-x}As$.

Parameter	Values	Ref.	Parameter	Values	Ref.
$\chi_0, x < 0.45$ (eV)	$4.07 - 1.1x$	[49]	$\mu_n, x < 0.45$ (cm^2/s/V)	$(8 - 22x + 10x^2) \times 10^3$	[49]
$\chi_0, x \geq 0.45$ (eV)	$3.64 - 0.14x$	[49]	$\mu_n, x \geq 0.45$ (cm^2/s/V)	$-255 + 1160x - 720x^2$	[49]
$\varepsilon_{r,s}$	$12.90 - 2.84x$	[49]	$\mu_{p,300}$ (cm^2/s/V)	$370 - 970x + 740x^2$	[49]
$E_{g0,\Gamma}$ (eV)	$1.519 + 1.115x + 0.37x^2$	[49]	$\beta_{\mu,n}$	0.75	fit
$E_{g0,X}$ (eV)	$1.981 + 0.124x + 0.144x^2$	[49]	$\beta_{\mu,p}$	0.75	fit
$E_{g0,L}$ (eV)	$1.815 + 0.69x$	[49]	$\tau_{n,300}^{SRH}$ (ns)	1	fit
β_g (K)	204	[49]	$\tau_{p,300}^{SRH}$ (ns)	1	fit
α_Γ (eV/K)	5.41×10^{-4}	[49]	β_{SRH}	1	fit
α_X (eV/K)	4.6×10^{-4}	[49]	B^{rad} (cm^3/s)	1.8×10^{-10}	[49]
α_L (eV/K)	6.05×10^{-4}	[49]	C_n^{Aug} (cm^6/s)	5×10^{-31}	fit
α_χ (eV/K)	2.75×10^{-4}	[49]	C_p^{Aug} (cm^6/s)	3.75×10^{-31}	fit
ΔE_A		[63]	κ_{air} (W/m/K)	0.025	[49]
ΔE_D (eV)		[63]	κ_{cavity} (W/m/K)	7.8 (13)	fit
m_Γ/m_0	$0.067 + 0.083x$	[64]	$\kappa_{mirror,t}$ (W/m/K)	11.6 (14.5)	fit
m_X/m_0	$0.850 - 0.140x$	[64]	$\kappa_{mirror,z}$ (W/m/K)	9.3 (15.5)	fit
m_L/m_0	$0.560 + 0.100x$	[64]	$\kappa_{substrate}$ (W/m/K)	27.6 (46)	fit
m_p/m_0	$0.5 + 0.29x$	[65]	κ_{passiv} (W/m/K)	0.4 (0.5)	fit
$\tau_{scat,n}$ (ps)	10	fit	κ_{metal} (W/m/K)	300	[49]
$\tau_{scat,p}$ (ps)	5	fit	β_T	1.30	[66]
n_{AlGaAs}		[67]	$\frac{dn}{dT}$ (1/K)	2	[67]

4 Conclusions and future work

This paper presents the application of our VCSEL electro-opto-thermal numerical simulator VENUS to a standard multimode device realized and characterized at Philips Photonics. In particular, we focus on the insights and outcomes of the quantum-corrected drift-diffusion model, clarifying its fundamental role in predicting the VCSEL characteristics.

One of the effects of quantum corrections is the generation of an electron vortex in the active region, which appears when realistic carrier transport parameters are used. A thorough discussion of the phenomenon is presented, showing how it doesn't lead to any physical contradiction and proposing possible validation strategies.

Having demonstrated in this paper the model validity through extensive comparisons with experimental results in static conditions, future works will deal with the prediction of the dynamic and noise properties of VCSELs.

5 Acknowledgments

A Material parameters of $Al_xGa_{1-x}As$

This appendix provides some details about the material parameters used in the simulations presented in this work.

The bandgap thermal dependence is modeled as

$$E_{\mathrm{g}} = E_{\mathrm{g},0} - \alpha_{\mathrm{g}} \frac{T^2}{\beta_{\mathrm{g}} + T}. \tag{8}$$

Starting from this expression, the densities of states are evaluated by a many-valley description [33].

The mobility dependence on doping impurity concentrations is described by a modified Hilsum model [50] calibrated on experimental values

$$\mu_{n/p,300} = \frac{\mu_{n/p,\mathrm{int}}}{1 + \left(\frac{N_A + N_D}{N_X}\right)^{0.35}}, \tag{9}$$

where $\mu_{n/p,\mathrm{int}}$ indicates the mobility of the intrinsic material, N_D and N_A are the donor and acceptor doping concentrations, and N_X is a fitting parameter; in our simulations, $N_X = 4 \times 10^{17}\,\mathrm{cm}^{-3}$.

The thermal dependence of mobility is described by the following expression:

$$\mu_{n/p} = \mu_{n/p,300} \left(\frac{T}{300\,\mathrm{K}}\right)^{-\beta_{\mu,n/p}}. \tag{10}$$

The SRH lifetimes exhibit a similar temperature dependence:

$$\tau_{n/p}^{\mathrm{SRH}} = \tau_{n/p,300} \left(\frac{T}{300\,\mathrm{K}}\right)^{-\beta_{\mathrm{SRH}}}. \tag{11}$$

References

1. R. Michalzik, Ed., VCSELs: Fundamentals, Technology and Applications of Vertical-Cavity Surface-Emitting Lasers. Berlin: Springer-Verlag, 2013.
2. H. Moench, M. Carpaij, P. Gerlach, S. Gronenborn, R. Gudde, J. Hellmig, J. Kolb, and A. van der Lee, "VCSEL based sensors for distance and velocity," in Proc. SPIE 9766, Mar. 2016, pp. 97 660A–1–16.
3. K. J. Ebeling, R. Michalzik, and H. Moench, "Vertical-cavity surface-emitting laser technology applications with focus on sensors and three-dimensional imaging," Japan. J. Appl. Phys., vol. 52, pp. 08PA02–1–11, 2018.
4. M. Kuramoto, S. Kobayashi, T. Akagi, K. Tazawa, K. Tanaka, T. Saito, and T. Takeuchi, "Enhancement of slope efficiency and output power in GaN-based vertical-cavity surface-emitting lasers with a SiO$_2$-buried lateral index guide," Appl. Phys. Lett., vol. 12, pp. 111 104–1–4, 2018.
5. M. Fill, P. Debernardi, F. Felder, and H. Zogg, "Lead-chalcogenide mid-infrared vertical external cavity surface emitting lasers with improved threshold: Theory and experiment," Appl. Phys. Lett., vol. 103, pp. 201 120–1–3, 2013.
6. A. Tibaldi, P. Debernardi, and R. Orta, "High-contrast grating performance issues in tunable VCSELs," IEEE J. Quantum Electron., vol. 51, no. 12, p. 2400407, 2015.
7. W. W. Bewley, C. L. Canedy, C. S. Kim, C. D. Merritt, M. V. Warren, I. Vurgaftman, J. R. Meyer, and M. Kim, "Room-temperature mid-infrared interband cascade vertical-cavity surface-emitting lasers," Appl. Phys. Lett., vol. 109, pp. 151 108–1–5, 2016.
8. G. P. Bava, P. Debernardi, and L. Fratta, "Three-dimensional model for vectorial fields in vertical-cavity surface-emitting lasers," Phys. Rev. A, vol. 63, no. 2, p. 23816, 2001.
9. P. Debernardi and G. P. Bava, "Coupled mode theory: a powerful tool for analyzing complex VCSELs and designing advanced devices features," IEEE J. Select. Topics Quantum Electron., vol. 9, no. 3, pp. 905–917, 2003.
10. P. Debernardi, "HOT-VELM: a comprehensive and efficient code for fully vectorial and 3-D hot-cavity VCSEL simulation," IEEE J. Quantum Electron., vol. 45, no. 8, pp. 979–992, 2009.
11. P. Bienstman, R. Baets, J. Vukusic, A. Larsson, M. J. Noble, M. Brunner, K. Gulden, P. Debernardi, L. Fratta, G. P. Bava, H. Wenzel, B. Klein, O. Conradi, R. Pregla, S. A. Riyopoulos, J.-F. P. Seurin, and S. L. Chuang, "Comparison of optical VCSEL models on the simulation of oxide-confined devices," IEEE J. Quantum Electron., vol. 37, no. 12, pp. 1618–1631, 2001.
12. P. Debernardi, G. P. Bava, C. Degen, I. Fischer, and W. Elsäßer, "Influence of anisotropies on transverse modes in oxide-confined VCSELs," IEEE J. Quantum Electron., vol. 38, no. 1, pp. 73–84, 2002.

13. P. Debernardi, G. P. Bava, F. Monti di Sopra, and M. B. Willemsen, "Features of vectorial modes in phase-coupled VCSEL arrays: experiments and theory," IEEE J. Quantum Electron., vol. 39, no. 1, pp. 109–119, 2003.

14. P. Debernardi, J. M. Ostermann, M. Sondermann, T. Ackemann, G. P. Bava, and R. Michalzik, "Theoretical-experimental study of the vectorial modal properties of polarization-stable multimode grating VCSELs," IEEE J. Select. Topics Quantum Electron., vol. 13, no. 5, pp. 1340–1348, 2007.

15. P. Debernardi, R. Orta, T. Gründl, and M.-C. Amann, "3-D vectorial optical model for high-contrast grating vertical-cavity surface-emitting lasers," IEEE J. Quantum Electron., vol. 49, no. 2, pp. 137–145, 2013.

16. R. Orta, A. Tibaldi, and P. Debernardi, "Bimodal resonance phenomena–part I: generalized Fabry–Pérot interferometers," IEEE J. Quantum Electron., vol. 52, no. 12, pp. 6 100 508–1–8, 2016.

17. A. Tibaldi, P. Debernardi, and R. Orta, "Bimodal resonance phenomena–part III: high-contrast grating reflectors," IEEE J. Quantum Electron., vol. 54, no. 6, pp. 6 600 108–1–8, 2018.

18. P. Debernardi, A. Tibaldi, P. Gerlach, P. Martelli, P. Boffi, M. Martinelli, D. Coviello, and R. Orta, "Modal performance of spiral phase plate VCSELs," IEEE J. Quantum Electron., vol. 52, no. 5, pp. 2 400 108–1–8, 2016.

19. X. Zhou, F. Bertazzi, M. Goano, G. Ghione, and E. Bellotti, "Deriving $k \cdot p$ parameters from full-Brillouin-zone descriptions: A finite-element envelope function model for quantum-confined wurtzite nanostructures," J. Appl. Phys., vol. 116, no. 3, p. 033709, July 2014.

20. B. A. Foreman, "Elimination of spurious solutions from eight-band $k \cdot p$ theory," Phys. Rev. B, vol. 56, no. 20, pp. R12 748–R12 751, Nov. 1997.

21. A. Tomita and A. Suzuki, "A new density matrix theory for semiconductor lasers, including non-Markovian intraband relaxation and its application to nonlinear gain," IEEE J. Quantum Electron., vol. 27, no. 6, pp. 1630–1641, 1991.

22. C. Canuto, M. Y. Hussaini, A. Quarteroni, and T. A. Zang, Spectral methods: evolution to complex geometries and applications to fluid dynamics, 1st ed. Berlin: Springer-Verlag, 2007.

23. A. Tibaldi, R. Orta, O. A. Peverini, G. Addamo, G. Virone, and R. Tascone, "Skew incidence plane-wave scattering from 2-D dielectric periodic structures: analysis by the mortar-element method," IEEE Trans. Microwave Theory Tech., vol. 63, no. 1, pp. 11–19, 2015.

24. F. Bertazzi, M. Moresco, and E. Bellotti, "Theory of high field carrier transport and impact ionization in wurtzite GaN. Part I: A full band Monte Carlo model," J. Appl. Phys., vol. 106, no. 6, p. 063718, Sept. 2009.

25. F. Bertazzi, M. Moresco, M. Penna, M. Goano, and E. Bellotti, "Full-band Monte Carlo simulation of HgCdTe APDs," J. Electron. Mater., vol. 39, no. 7, pp. 912–917, 2010.

26. E. Bellotti, F. Bertazzi, S. Shishehchi, M. Matsubara, and M. Goano, "Theory of carriers transport in III-nitride materials: State of the art and future outlook," IEEE Trans. Electron Devices, vol. 60, no. 10, pp. 3204–3215, Oct. 2013.

27. M. Goano, F. Bertazzi, X. Zhou, M. Mandurrino, S. Dominici, M. Vallone, G. Ghione, A. Tibaldi, M. Calciati, P. Debernardi, F. Dolcini, F. Rossi, G. Verzellesi, M. Meneghini, N. Trivellin, C. De Santi, E. Zanoni, and E. Bellotti, "Challenges towards the simulation of GaN-based LEDs beyond the semi-classical framework," in SPIE Photonics West, Physics and Simulation of Optoelectronic Devices XXIV, B. Witzigmann, M. Osiński, and Y. Arakawa, Eds., vol. 9742, Proceedings of the SPIE, San Francisco, CA, Feb. 2016, p. 974202.

28. F. Bertazzi, M. Goano, G. Ghione, A. Tibaldi, P. Debernardi, and E. Bellotti, "Electron transport," in Handbook of Optoelectronic Device Modeling and Simulation, J. Piprek, Ed. Boca Raton, FL: CRC Press, 2017, ch. 2, pp. 35–80.

29. F. Bertazzi, F. Cappelluti, S. Donati Guerrieri, F. Bonani, and G. Ghione, "Self-consistent coupled carrier transport full-wave EM analysis of semiconductor traveling-wave devices," IEEE Trans. Microwave Theory Tech., vol. 54, no. 4, pp. 1611–1618, Appl. Phys. Rev. 2006.

30. G. Ghione and A. Benvenuti, "Discretization schemes for high-frequency semiconductor device models," IEEE Trans. Antennas Propagation, vol. AP-45, no. 3, pp. 443–456, Mar. 1997.

31. D. L. Scharfetter and H. K. Gummel, "Large-signal analysis of a silicon read diode transistor," IEEE Trans. Electron Devices, vol. ED-16, no. 1, pp. 64–77, Jan. 1969.

32. P. Debernardi, "Three-dimensional modeling of VCSELs," in VCSELs: Fundamentals, Technology and Applications of Vertical-Cavity Surface-Emitting Lasers, R. Michalzik, Ed. Berlin: Springer-Verlag, 2013, ch. 3, pp. 77–117.

33. M. Calciati, A. Tibaldi, F. Bertazzi, M. Goano, and P. Debernardi, "Many-valley electron transport in AlGaAs VCSELs," Semiconductor Sci. Tech., vol. 32, no. 5, p. 055007, 2017.

34. A. Tibaldi, F. Bertazzi, M. Goano, R. Michalzik, and P. Debernardi, "VENUS: a Vertical-cavity surface-emitting laser Electro-opto-thermal NUmerical Simulator," IEEE J. Select. Topics Quantum Electron., vol. 25, no. 6, p. 1500212, Nov./Dec. 2019.

35. N. Tessler and G. Eisenstein, "On carrier injection and gain dynamics in quantum well lasers," IEEE J. Quantum Electron., vol. QE-29, no. 6, pp. 1586–1595, June 1993.

36. G. A. Baraff, "Semiclassical description of electron transport in semiconductor quantum-well devices," Phys. Rev. B, vol. 55, no. 16, pp. 10 745–10 753, 1997.

37. ——, "Model for the effect of finite phase-coherence length on resonant transmission and capture by quantum wells," Phys. Rev. B, vol. 58, no. 20, pp. 13 799–13 810, Nov. 1998.

38. M. S. Hybertsen, B. Witzigmann, M. A. Alam, and R. K. Smith, "Role of carrier capture in microscopic simulation of multi-quantum-well semiconductor laser diodes," J. Comp. Electron., vol. 1, no. 1, pp. 113–118, 2002.

39. M. Alam, M. S. Hybertsen, R. Smith, and G. Baraff, "Simulation of semiconductor quantum well lasers," IEEE Trans. Electron Devices, vol. 47, no. 10, pp. 1917–1925, Oct. 2000.

40. M. Grupen and K. Hess, "Simulation of carrier transport and nonlinearities in quantum-well laser diodes," IEEE J. Quantum Electron., vol. 34, no. 1, pp. 120–140, Jan. 1998.

41. B. Witzigmann, A. Witzig, and W. Fichtner, "A multidimensional laser simulator for edge-emitters including quantum carrier capture," IEEE Trans. Electron Devices, vol. 47, no. 10, pp. 1926–1934, Oct. 2000.

42. M. Streiff, A. Witzig, M. Pfeiffer, P. Royo, and W. Fichtner, "A comprehensive VCSEL device simulator," IEEE J. Select. Topics Quantum Electron., vol. 9, no. 3, pp. 879–891, 2003.

43. M. Gioannini, A. P. Cédola, N. Di Santo, F. Bertazzi, and F. Cappelluti, "Simulation of quantum dot solar cells including carrier intersubband dynamics and transport," IEEE J. Photovoltaics, vol. 3, no. 4, pp. 1271–1278, 2013.

44. A. P. Engelhardt, J. S. Kolb, F. Roemer, U. Weichmann, H. Moench, and B. Witzigmann, "Temperature-dependent investigation of carrier transport, injection, and densities in AlGaAs-based multi-quantum-well active layers for vertical-cavity surface-emitting lasers," Opt. Eng., vol. 54, no. 1, pp. 016 107–1–10, 2015.

45. M. Vallone, F. Bertazzi, M. Goano, and G. Ghione, "Carrier capture in InGaN/GaN quantum wells: Role of electron-electron scattering," J. Appl. Phys., vol. 121, no. 12, p. 123107, Mar. 2017.

46. C. De Santi, M. Meneghini, A. Tibaldi, M. Vallone, M. Goano, F. Bertazzi, G. Verzellesi, G. Meneghesso, and E. Zanoni, "Physical mechanisms limiting the performance and the reliability of GaN-based LEDs," in Nitride Semiconductor Light-Emitting Diodes, 2nd ed., J. J. Huang, H. C. Kuo, and S.-C. Shen, Eds. Duxford, U.K.: Woodhead Publishing, 2018, ch. 14, pp. 455–489.

47. D. Schroeder, Modelling of Interface Carrier Transport for Device Simulation, ser. Computational Microelectronics.   Wien: Springer-Verlag, 1994.

48. P. Debernardi, A. Kroner, F. Rinaldi, and R. Michalzik, "Surface relief versus standard VCSELs: a comparison between experimental and hot-cavity model results," IEEE J. Select. Topics Quantum Electron., vol. 15, no. 3, pp. 828–837, 2009.

49. "Physical properties of semiconductors," Ioffe Physico-Technical Institute, St. Petersburg, Russia. [Online]. Available: http://www.ioffe.ru/SVA/NSM/Semicond/index.html

50. C. Hilsum, "Simple empirical relationship between mobility and carrier concentration," Electron. Lett., vol. 10, no. 13, pp. 259–260, 1974.

51. R. Gottinger, A. Gold, G. Abstreiter, G. Weimann, and W. Schlapp, "Interface roughness scattering and electron mobilities in thin GaAs quantum wells," Europhys. Lett., vol. 1988, no. 2, pp. 183–188, 1988.

52. H. Sakaki, T. Noda, K. Hirakawa, M. Tanaka, and T. Matsusue, "Interface roughness scattering in GaAs/AlAs quantum wells," Appl. Phys. Lett., vol. 51, no. 23, pp. 1934–1936, 1987.

53. T. Ando, "Self-consistent results for a GaAs/$Al_x Ga_{1-x}$As heterojunction. II. low temperature mobility," J. Phys. Soc. Japan, vol. 51, no. 12, pp. 3900–3907, 1982.

54. J.-P. Tetienne, N. Dontschuk, D. A. Broadway, A. Stacey, D. A. Simpson, and L. C. L. Hollenberg, "Quantum imaging of current flow in graphene," Sci. Adv., vol. 3, no. 4, p. e1602429, 2017.

55. S. Bhandari, G. H. Lee, K. Watanabe, T. Taniguchi, P. Kim, and R. M. Westervelt, "Imaging electron flow from collimating contacts in graphene," 2D Mater., vol. 5, no. 2, p. e1602429, 2018.

56. L. Ella, A. Rozen, J. Birkbeck, M. Ben-Shalom, D. Perello, J. Zultak, T. Taniguchi, K. Watanabe, A. K. Geim, S. Ilani, and J. A. Sulpizio, "Simultaneous voltage and current density imaging of flowing electrons in two dimensions," Nature Nanotech., vol. 14, pp. 480–487, 2019.

57. W. Rauch, E. Gornik, G. Weimann, and W. Schlapp, "Scattering mechanisms in inverted AlGaAs-GaAs heterostructures studied by magnetotransport measurements," J. Appl. Phys., vol. 70, p. 6860, 1991.

58. M. J. Yoo, T. A. Fulton, H. F. Hess, R. L. Willett, L. N. Dunkleberger, R. J. Chichester, L. N. Pfeiffer, and K. W. West, "Scanning single-electron transistor microscopy: imaging individual charges," Science, vol. 276, no. 5312, pp. 579–582, 1997.

59. F. Bertazzi, M. Goano, and E. Bellotti, "Calculation of Auger lifetime in HgCdTe," J. Electron. Mater., vol. 40, no. 8, pp. 1663–1667, 2011.

60. M. Calciati, M. Goano, F. Bertazzi, M. Vallone, X. Zhou, G. Ghione, M. Meneghini, G. Meneghesso, E. Zanoni, E. Bellotti, G. Verzellesi, D. Zhu, and C. Humphreys, "Correlating electroluminescence characterization and physics-based models of InGaN/GaN LEDs: Pitfalls and open issues," AIP Adv., vol. 4, no. 6, p. 067118, June 2014.

61. F. Bertazzi, M. Goano, X. Zhou, M. Calciati, G. Ghione, M. Matsubara, and E. Bellotti, "Looking for Auger signatures in III-nitride light emitters: A full-band Monte Carlo perspective," Appl. Phys. Lett., vol. 106, no. 6, p. 061112, Feb. 2015.

62. J. Piprek, "What limits the efficiency of high-power InGaN/GaN lasers?" IEEE J. Quantum Electron., vol. 53, no. 1, pp. 1–4, Feb. 2017.

63. L. Pavesi and M. Guzzi, "Photoluminescence of $Al_xGa_{1-x}As$ alloys," J. Appl. Phys., vol. 75, no. 10, pp. 4779–4842, 1994.

64. S. Adachi, "GaAs, AlAs, and $Al_xGa_{1-x}As$: Material parameters for use in research and device applications," J. Appl. Phys., vol. 58, no. 3, pp. R1–R29, Aug. 1985.

65. S. L. Chuang, Physics of Photonic Devices. Hoboken: John Wiley & Sons, 2009.

66. S. Adachi, Ed., Properties of Aluminium Gallium Arsenide, ser. EMIS Datareviews Series. London: INSPEC, 1993.

67. S. W. Corzine, "Design of vertical-cavity surface-emitting lasers with strained and unstrained quantum well active regions," Ph.D. dissertation, University of California, Santa Barbara, 1993.